Paleoceanography and Paleoclimatology

AGU ADVANCING EARTH AND SPACE SCIENCES

RESEARCH ARTICLE
10.1029/2022PA004522

Dynamics of the Marine Dissolved Organic Carbon Reservoir in Glacial Climate Simulations: The Importance of Biological Production

Maya D. Gilchrist[1] **and Katsumi Matsumoto**[1]

[1]Department of Earth and Environmental Sciences, University of Minnesota, Twin Cities, Minneapolis, MN, USA

Key Points:

- The marine dissolved organic carbon (DOC) reservoir is mobile in response to glacial climate forcing and rapid changes in the meridional overturning circulation
- Changes in the size of the DOC reservoir are primarily driven by changes in DOC production rather than DOC degradation
- Marine DOC cycling is directly related to atmospheric pCO_2 over simulated climate change events

Supporting Information:

Supporting Information may be found in the online version of this article.

Correspondence to:

M. D. Gilchrist,
mayagilchrist@gmail.com

Citation:

Gilchrist, M. D., & Matsumoto, K. (2023). Dynamics of the marine dissolved organic carbon reservoir in glacial climate simulations: The importance of biological production. *Paleoceanography and Paleoclimatology*, *38*, e2022PA004522. https://doi.org/10.1029/2022PA004522

Received 25 JUL 2022
Accepted 4 JUL 2023

Abstract The marine dissolved organic carbon (DOC) reservoir rivals the atmospheric carbon inventory in size. Recent work has suggested that the size of the DOC reservoir may respond to variations in sea temperature and global overturning circulation strength. Moreover, mobilization of marine DOC has been implicated in paleoclimate events including Cryogenian glaciation and Eocene hyperthermals. Despite these suggestions, the dynamics of the marine DOC reservoir are poorly understood, and previous carbon cycle modeling has generally assumed this reservoir to be static. In this study, we utilize an Earth system model of intermediate complexity to assess the response of the marine DOC reservoir to various glacial boundary conditions. Our results indicate that the marine DOC reservoir is responsive to glacial perturbations and may shrink or expand on the order of 10–100 Pg C. In contrast to recent studies that emphasize the importance of DOC degradation in driving the mobility of DOC reservoir, our study indicates the importance of DOC production. In the experiment under full glacial boundary conditions, for example, a 19% drop in net primary production leads to an 81 Pg C reduction in the DOC pool, without which the atmospheric CO_2 concentration would have been lower by approximately 38 ppm by dissolved inorganic carbon changes alone. Thus, DOC reservoir variability is necessary to fully account for the simulated changes in atmospheric CO_2 concentration. Our findings based on glacial experiments are corroborated in a different set of simulations using freshwater flux to induce weakening of the Atlantic meridional overturning circulation.

Plain Language Summary There is a significant reservoir of dissolved organic carbon (DOC) in the ocean originating from the production and decay of microbes, nearly equal to the amount of carbon contained as carbon dioxide (CO_2) in the atmosphere. Studies have suggested that the total amount of DOC in the ocean may respond to climate effects on ocean temperatures and circulation, and that releases of DOC from the ocean as CO_2 to the atmosphere may have contributed to some climate change events in Earth's history. To date, however, little modeling work has been done to understand this suggestion. In this study, we used a computer model of the earth's ocean and atmosphere to simulate the response of marine DOC to climate conditions representing the height of Earth's last glacial period. We found that the total amount of marine DOC simulated in our model could vary in response to the specific climate conditions applied and the modeled impacts on ocean biological production. Importantly, we found that these changes in the DOC reservoir are sufficiently large that without it, changes in atmospheric CO_2 levels cannot be fully understood. Our results suggest that understanding marine DOC is crucial in understanding global climate changes throughout Earth's history.

1. Introduction

Biological production in the ocean exerts an important control on atmospheric CO_2. It has been suggested that without marine biological activity, modern atmospheric CO_2 concentrations would be higher by approximately 200–300 ppm (Broecker & Peng, 1982). This sequestration process is predominantly fueled by photoautotrophic phytoplankton production in the sunlit portion of the upper ocean, which yields organic matter in the particulate (POM) and dissolved (DOM) forms. While POM sinks through the water column, DOM is passively transported through the ocean by global circulation, accumulating in the subsurface along deep-water pathways (Hansell, 2013). At 662 Pg C, this pool of marine DOC represents the largest reservoir of reduced carbon in the ocean, containing >200 times the carbon contained in marine biomass (Hansell et al., 2009) and rivaling the atmospheric carbon inventory (594 Pg C in the preindustrial; 860 Pg C presently). For context, the amount of additional carbon in the pool of dissolved inorganic carbon (DIC) due to the organic carbon pump (i.e., respired

carbon) is estimated to be approximately 1,672 Pg C (Williams & Follows, 2011), which is only two to three times the DOC reservoir.

DOC is produced in the surface ocean at a rate of up to 28 Pg C yr^{-1} (Hansell, 2013), most of which is biologically labile and respired to CO_2 in support of the microbial loop on the order of hours to days. Due to its short lifetime, this highly labile DOC pool is virtually unobservable, but a recalcitrant portion escapes rapid remineralization and accumulates throughout the ocean. The observable, more recalcitrant pool of DOC can be characterized on a wide spectrum of reactivity to biotic or abiotic degradation processes. Hansell defines four broad, operational fractions of recalcitrant DOC. From most reactive to least reactive to degradation mechanisms, these are: semi-labile (DOC_{SL}), semi-refractory, refractory (DOC_R), and ultra-refractory, which have lifetimes ranging from months to tens of thousands of years. The more labile fractions of DOC are primary confined to the mesopelagic zone (upper ~1,000 m), while DOC_R is distributed throughout the water column and dominates the deep ocean (Hansell, 2013; Wagner et al., 2020).

Binning DOC into recalcitrance fractions is convenient for conceptualization, but DOC is chemically and structurally diverse, consisting of thousands to millions of organic compounds differing in composition, concentration, source, age, and degradation history. Due to its complexity, it is poorly characterized, and many questions remain regarding mechanisms of its production, transformation, and removal (Wagner et al., 2020). Accordingly, there are multiple explanations for the range in observations of apparent DOC recalcitrance. A prevailing hypothesis is the size-reactivity continuum hypothesis, which proposes that a molecularly large, young, labile pool of DOC in surface waters becomes increasingly and intrinsically recalcitrant as it is broken down, resulting in accumulation of relatively small, old, refractory DOC molecules in the interior ocean (Benner & Amon, 2015; Walker et al., 2016). An alternative explanation is the dilution hypothesis (Arrieta et al., 2015), which proposes that refractory DOC is not inherently resistant to degradation, but rather that there are so many structurally and chemically different DOC compounds that any one of them would occur in a very low or dilute concentration in the deep ocean. Since heterotrophic microbes cannot break down all DOC compounds but target compounds with specific enzymes, the low concentrations of any one compound make it too energetically expensive for heterotrophs to seek and consume that compound, thus allowing most DOC in the deep ocean to escape microbial breakdown (Arrieta et al., 2015). Another suggestion explains DOC recalcitrance as a function of mismatch between DOC characteristics and the needs of surrounding heterotrophic microbial communities (Carlson et al., 2004). This suggestion has been extended to a more unifying hypothesis that functionally refractory DOC can be converted to more labile forms by changes in community composition and environmental variables (Zakem et al., 2021).

At least 95% of the total marine DOC reservoir is either functionally or inherently refractory (~630 Pg C) and very aged relative to ocean overturning rates (Williams & Druffel, 1987). Removal rates indicate that throughout the ocean, DOC_R persists for roughly 16,000 years (Hansell, 2013). Follett et al. (2014) suggests that the removal time scale is even longer at 30,000 years for isotopically depleted DOC, which may be closer to what Hansell (2013) calls ultra-refractory DOC with a turnover time scale of approximately 40,000 years. Because of the slow turnover of DOC_R, until recently, the role of marine DOC in the global carbon cycle was thought to be limited. However, there is evidence for the mobilization of DOC_R contributing to paleoclimate change events. Rothman et al. (2003) attributed the most significant negative carbon isotope excursion ($\delta^{13}C$) of the Neoproterozoic (1,000–543 Ma) to increased remineralization of an unusually large pool of DOC relative to DIC. Remineralization of an expanded DOC pool has also been implicated in preventing the onset of a Snowball Earth at the end of Cryogenian glaciation (635 Ma) (Peltier et al., 2007; Swanson-Hysell et al., 2010). From the isotope data in marine sediment records, it has been proposed that rapid ventilation of DIC oxidized from the marine DOC_R pool contributed to Middle and Early Eocene (~50–47.5 Ma) hyperthermal events (Sexton et al., 2011). Furthermore, fluctuations in the DOC reservoir have been proposed to explain the 400-kyr cycles in $\delta^{13}C$ that have been widely observed in pre-Quaternary biogeochemical records (Ma et al., 2017; Wang et al., 2014). This growing body of work suggests a marine DOC dynamic that is both responsive to and influential of global carbon reorganization.

More recently, it has been suggested that the size of the total marine DOC reservoir may change in response to future warming, although there is considerable uncertainty in the magnitude, direction, and driving mechanisms behind such changes (Wagner et al., 2020). One hypothesis is that rising ocean temperatures could stimulate DOC removal by temperature-dependent microbial degradation processes, which could lead to a 7 Pg C reduction in the total DOC reservoir under a uniform 1°C warming scenario (Lønborg et al., 2018). Another study hypothesizes that a weakening of global overturning circulation could reduce the exposure of

interior-ocean DOC to surface-level degradation process, thereby leading to an accumulation of DOC over time and providing a negative feedback to rising atmospheric CO_2 levels (Shen & Benner, 2018). Despite these speculations, little is known about the temporal dynamics of marine DOC over timescales relevant to global climate changes. In part due to its long lifetime, it is difficult to achieve a steady state representation of DOC in high-resolution, global scale carbon cycle models. Quantitative uncertainty in the balance between observed DOC production and removal mechanisms in the global ocean provides additional challenges (Wagner et al., 2020).

In this study, we attempt to resolve the oceanic DOC distribution in an Earth system model of intermediate complexity (EMIC). We take advantage of the size-reactivity continuum hypothesis, representing the reactivity spectrum of observable DOC using two endmembers, DOC_{SL} and DOC_R, following Williams and Druffel (1987). Following the implementation of environmentally-dependent DOM production and removal mechanisms and calibration with respect to observed spatial distribution and stoichiometry, we assess the response of the marine DOC reservoir to climate perturbations representative of the last glacial period.

The last glacial period is characterized by atmospheric pCO_2 levels 80–100 ppm lower than the preindustrial Holocene and is punctuated by alternations between warm interstadials and cool interstadials (Bereiter et al., 2015). Paleoclimate records based on ice-rafted debris for some of these northern hemisphere stadials (Heinrich Stadials) show evidence of massive discharges of icebergs from the Laurentide Ice Sheet into the North Atlantic Ocean (Bond et al., 1992). Freshwater input from the icebergs adds buoyancy to the surface ocean, which may have triggered reductions in the strength of the Atlantic meridional overturning circulation (AMOC), including near-total collapse of the AMOC associated with deglacial stadials (McManus et al., 2004).

Here, we simulate glacial climate conditions and AMOC weakening using our new DOC-enabled EMIC, with the goal of understanding the response of the marine DOC inventory to climate change. This work builds on our previous glacial modeling study, which used an earlier version of the model but focused on the effects of flexible phytoplankton stoichiometry on atmospheric pCO_2 (Matsumoto et al., 2020). Our previous work did not consider the large DOC_R pool and thus implicitly assumed, as commonly done, that changes in atmospheric pCO_2 are accounted for solely by changes in marine DIC. Modeling work using the Grid ENabled Integrated Earth system model (GENIE), however, suggests the potential for a reduced Last Glacial Maximum (LGM) DOC reservoir to contribute to an increase in atmospheric pCO_2 that partially offsets stratification and solubility effects on carbon sequestration (Ma & Tian, 2014). By quantifying DOC changes over these events in our model, we attempt to gain a more complete understanding of the relationship between atmospheric and ocean carbon cycling processes.

2. Model and Experiments

For this study, we used a newly updated version of the Minnesota Earth System Model for Biogeochemistry (MESMO), which has a 3D dynamical ocean model, a 2D energy-moisture balanced model of the atmosphere, and a 2D dynamic and thermodynamic model of sea ice (Matsumoto et al., 2008, 2013, 2021). Previous versions of MESMO have been used in multiple investigations of the global carbon cycle under past, present and future conditions (e.g., Matsumoto et al., 2020; Matsumoto & Yokoyama, 2013; Tanioka & Matsumoto, 2017) and have participated in model intercomparison projects (e.g., Archer et al., 2009; Joos et al., 2013; and Weaver et al., 2012). Here, we limit the model description to new DOC features of MESMO.

The version of MESMO used in this study, MESMO 3c, was adapted from MESMO 3 (Matsumoto et al., 2021) and calibrated with respect to DOM cycling features. The net primary production (NPP) has not changed in the model, but the DOM production that immediately follows NPP and the temperature dependent DOM degradation rates used in this study are unique to MESMO 3c and described in Sections 2.1 and 2.2. The remaining set of physical and biogeochemical equations governing this model have been carried over from MESMO 3 and are described by Matsumoto et al. (2021). It is important to note for this study that as an EMIC, MESMO 3c is capable of running to steady state within a day (~1 hr walltime/1,000 years of simulation). By comparison, it took the Community Earth System Model 7 months of walltime to simulate 6,010 years in a study of carbon isotopes (Jahn et al., 2015). The computational efficiency of MESMO is largely a result of its coarse ocean model resolution with 36 × 36 equal-area horizontal grid and 16 vertical levels. This efficiency renders MESMO 3c valuable in investigations of marine DOC, given the long timescales of DOC_R decay (16,000 years) and thus global ocean carbon cycle equilibration.

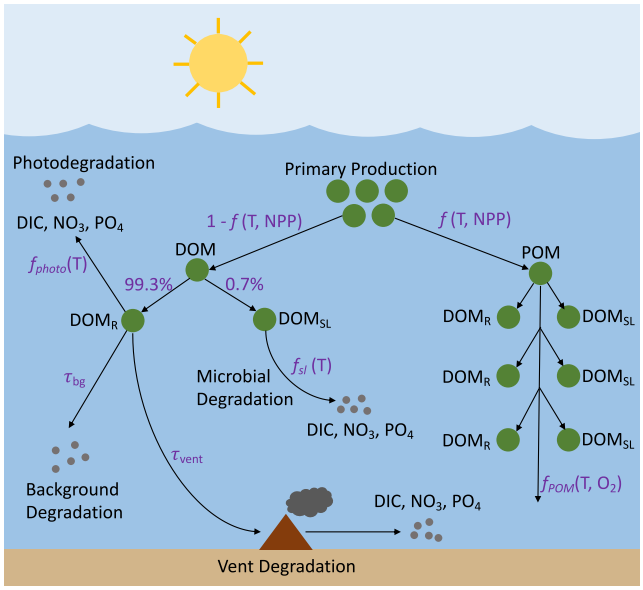

Figure 1. Schematic of DOM cycling in MESMO 3c. DOM is produced via NPP in the top 100 m and throughout the water column via the "deep POM split." DOM_{SL} is remineralized through temperature-dependent microbial degradation, and DOM_R is remineralized by temperature-dependent photodegradation at the surface, background degradation throughout the ocean, and transformation during passage through hydrothermal vents. DOP is remineralized preferentially to DON, which is remineralized preferentially to DOC, as described in Section 2.2.3.

2.1. Organic Matter Production

In MESMO 3c, NPP continues to occur in the top 100 m—represented by the first two depth levels of the model—and is carried out by three phytoplankton functional types (PFTs): eukaryotes, cyanobacteria, and diazotrophs. Production is dependent on ambient nutrient concentrations (N, P, Fe, and Si) and is limited by the nutrient in shortest supply relative to phytoplankton uptake stoichiometry. It also depends on light, temperature, and mixed layer depth (MLD). The full set of biogeochemical equations for phytoplankton production used in this model is described by Matsumoto et al. (2021).

New in MESMO 3c is that NPP is immediately routed to DOM and POM following a formulation for particle export ratio dependent on primary production, temperature, and euphotic zone depth (Dunne et al., 2005). Previously, in MESMO 3, we used the Laws et al. (2000) formula to calculate the fraction of NPP that is routed to POM (f_{POM}, unitless). However, the Laws formula has a dependence only on temperature, which gives f_{POM} a strong latitude dependence, making it unsuitable to model DOM production. Therefore, in MESMO 3c, we use Dunne et al. (2005)'s formula but adapt it to account for MESMO's global NPP lying at the low end of the possible range (34 Pg C yr^{-1}) (Table S3 in Supporting Information S1; Matsumoto et al., 2021). By increasing the temperature sensitivity of f_{POM} and adding a factor of 0.575 to the intercept in our adaptation of Dunne et al. (2005)'s formula, we are able to reproduce nearly the full range of observed f_{POM} values (Equation 1; Table S2 in Supporting Information S1).

$$f_{POM} = 3 \cdot (-0.01) \cdot T + 0.0582 \cdot \ln\left(\frac{1000 \cdot NPP}{Z_{eu}}\right) + 0.419 + 0.575 \quad (1)$$
$$0.04 < f_{POM} < 0.72$$

where:
T = temperature (°C),
NPP = net primary production (mol C m^{-2} y^{-1}),
Z_{eu} = depth of the euphotic zone (m).

DOM, which includes DOC, DON, DOP, and DOFe, is further split into semi-labile (DOM_{SL}) and recalcitrant (DOM_R) fractions at a ratio of 1,000:7 following Hansell (2013).

2.2. Organic Matter Removal

The "deep POM split" pathway of MESMO 3 is carried forward in MESMO 3c, whereby sinking POM is split or broken down into smaller POM and DOM (Figure 1). This POM pathway is motivated by observations that suggest that sinking POM dissolves (e.g., Smith et al., 1992) and as a result DOM concentrations at depths could be enhanced (Follett et al., 2014). The rate of POM splitting into DOM ($SPLIT_{POM}$, mol C kg^{-1} day^{-1}) depends on the availability of dissolved oxygen and temperature following Laufkötter et al. (2017):

$$SPLIT_{POM} = V_{POM} \cdot e^{k_R \cdot T \cdot \frac{[O_2]}{[O_2]+K_{O_2}}} \cdot [POM] \quad (2)$$

where
V_{POM} = base POM degradation rate (day^{-1}),
T = temperature (°C),
k_R = temperature sensitivity of remineralization ($°C^{-1}$),
k_{O2} = half-saturation constant for oxygen-dependent remineralization (μmol kg^{-1}).

$SPLIT_{POM}$, which represents the newly formed total DOM at depth, is further partitioned into DOM_{SL} and DOM_R at the same 1,000:7 ratio that occurs in the surface ocean. POM degradation to DOM—according to Equation 2—

is formulated to occur in the model without the loss of O_2. However, since much of this new DOM is routed to DOM_{SL}, which remineralizes quickly as discussed below, $SPLIT_{POM}$ effectively occurs with the loss of oxygen, thus justifying the remineralization formulation of Laufkötter et al. (2017). By explicitly converting POM to DOM before remineralization, the deep POM split pathway of MESMO 3 allows for a small but potentially important in situ source of DOM_R in the water column.

The fraction of POM that remains (i.e., POM- $SPLIT_{POM}$) represents POM that is now smaller and continues sinking deeper in the water column. Any POM that reaches the seafloor is remineralized directly to DIC and inorganic nutrients.

2.2.1. DOM_{SL} Remineralization

In MESMO 3c, microbial activity is assumed to remineralize DOM_{SL} within 1.5 years to DIC and inorganic nutrients (Hansell, 2013). The rate of DOM_{SL} remineralization ($R_{DOM_{SL}}$) is given by the product of DOM_{SL} and the inverse of timescale of decay (τ_{SL}) that has a temperature dependence (see Figure S1 in Supporting Information S1) according to:

$$\tau_{SL}{}^{-1} = 1.4001 \cdot e^{-0.041 \cdot T} \quad (3)$$

where

T = temperature in °C.

$$R_{DOM_{SL}} = \tau_{SL} \cdot [DOM_{SL}] \quad (4)$$

It has been long understood that phytoplankton metabolic rates increase as a function of temperature (i.e., Eppley, 1972), and thus, it is assumed that remineralization rates are also influenced by temperature (López-Urrutia et al., 2006). Equation 3 assumes a temperature dependence for biological remineralization similar to that of phytoplankton growth ($Q_{10} = 1.5$), where Q_{10} refers to the increase in metabolic rate per 10°C increase in temperature. This formulation yields a range in $\tau_{SL}{}^{-1}$ of 0.3 years for temperature of 36°C to 1.5 years for the seawater freezing temperature of −2°C (Figure S1 in Supporting Information S1).

2.2.2. DOM_R Remineralization

The three pathways of DOM_R remineralization in MESMO 3 are carried forward in MESMO 3c: (a) photodegradation in the top two euphotic levels (τ_{photo}), (b) slow, global background degradation (τ_{bg}), and (c) degradation during passage through hydrothermal vents (τ_{vent}). In MESMO 3c, these characteristic timescales of decay are calibrated, and τ_{photo} is now given a temperature dependence. The background and hydrothermal vent degradation occur respectively at uniform timescales of $\tau_{bg}{}^{-1} = 16{,}000$ years (Hansell, 2013) and $\tau_{vent}{}^{-1} << \Delta t$, where Δt is the biogeochemical model time step of 0.05 years. Therefore, τ_{vent} represents instantaneous removal of DOM_R in the volume of seawater that is assumed to circulate through the hydrothermal vents in a single model time step (Matsumoto et al., 2021). We adopted a global vent flux of 4.8×10^{16} kg yr^{-1} (Lang et al., 2006), which means that 0.0035% of the world ocean circulates through the vents each year and loses DOM_R. In the model, the global vent flux is distributed equally among the model grid boxes that contain the locations of mid ocean ridges.

Our implementation of a temperature-dependent photodegradation timescale for DOM_R is motivated by the significance of photodegradation as a DOC removal mechanism in the ocean (Mopper et al., 1991) coupled with recent laboratory observations that DOM photodegradation rates are strongly dependent on temperature (Molot & Dillon, 1997; Porcal et al., 2015). In MESMO 3c, photodegradation occurs in the surface (top 100 m) with a temperature dependence of $Q = 1.2$ (Equations 5 and 6). This formulation yields a range in $\tau_{photo}{}^{-1}$ of 36–70 years, the upper end of which represents the globally uniform photodegradation timescale proposed by Yamanaka and Tajika (1997) and previously used in MESMO 3 (Matsumoto et al., 2021).

$$\tau_{photo}{}^{-1} = 67.864z \cdot e^{-0.018 \cdot T} \quad (5)$$

where

T = temperature in °C.

The remineralization rate of DOM_R (R_{DOM_R}) is given by the product of DOM_R concentration and the inverse of the timescales of decay (τ_{bg}, τ_{photo}, τ_{vent}). The decay pathways are not necessarily exclusive and can be combined:

$$R_{DOM_R} = \left(\tau_{bg} + \tau_{photo} + \tau_{vent} \cdot \frac{SW_{flux\_local}}{SW_{grid}}\right) \cdot [DOM_R] \quad (6)$$

where
SW_{flux_local} = mass of seawater that circulates through the vents in each grid box in one timestep
SW_{grid} = total mass of seawater in the same grid box.

2.2.3. DOM Remineralization Stoichiometry

Observations indicate that marine DOM is enriched in C and N relative to the canonical Redfield ratio of 106:16:1, which has been explained by the preferential remineralization of DOP and DON relative to DOC (Letscher & Moore, 2015; Redfield, 1934). MESMO 3c implements the preferential remineralization of DOP over DON and DON over DOC for both the semi-labile and refractory pools, in accordance with the DOM stoichiometry estimates made by Letscher and Moore (2015) (Figure 1; Table S1 in Supporting Information S1). In MESMO 3c, DOP_{SL} and DON_{SL} are remineralized at 3 and 2 times the rate as DOC_{SL}, respectively, for microbially-mediated DOM_{SL} degradation. As for the refractory pools, DOP_R and DON_R are remineralized at 12 and 4 times the rate as DOC_R, respectively, for all DOM_R degradation mechanisms.

2.3. Experiments

We performed two sets of climate forcing experiments using MESMO 3c to assess the change in marine DOC inventory and spatial distribution: (a) application of glacial boundary conditions and (b) freshwater hosing in the North Atlantic. While the focus of this study is on the glacial simulations, we are motivated to conduct the second set of transient climate change experiments to demonstrate that some of our findings are seen in both sets of experiments and thus robust to the choice of the climate forcing. All climate experiments were run starting from the same model equilibrium state achieved after 20,000 years with the atmospheric pCO_2 fixed to the preindustrial value of 279 ppm. The two control runs for the two sets of experiments started from this equilibrium state, allowing atmospheric pCO_2 to freely vary, and served as reference to assess changes in physical and biogeochemical parameters in each sensitivity experiment.

2.3.1. Glacial Boundary Conditions

Following Matsumoto et al. (2020), we applied five boundary conditions representing well-documented physical parameters of LGM: (a) larger land ice coverage, (b) reduced infrared radiative forcing from greenhouse gases, (c) increased deposition of Fe-containing dust, (d) change in total insolation due to Earth's orbital parameters, and (e) weaker southern hemisphere westerly winds. The Laurentide and Fennoscandian Ice Sheets over North America and Eurasia are represented by a uniform land ice albedo in model grid boxes following LGM ice sheet reconstructions (Peltier, 1994). The LGM is also associated with reduced radiative forcing from greenhouse gases. The modeled radiative forcing was prescribed at -2.6 W m^{-2} to represent the difference in forcing from CO_2, methane (CH_4), and nitrous oxide (N_2O) between the LGM and late Holocene (Joos & Spahni, 2008). Dust flux into the ocean, and consequently Fe flux, were increased to represent the higher concentrations of dust in the LGM atmosphere (Mahowald et al., 2006). The modeled insolation received by the earth was adjusted in accordance with differences in orbital parameters during the LGM (Berger, 1978). Finally, we weakened the westerly wind stress poleward of 44°S by 50% as a proxy for reduced Southern Ocean ventilation, which is proposed to have contributed to the reduction in atmospheric pCO_2 during the LGM (e.g., Anderson et al., 2009). There is precedent for this wind treatment in glacial modeling studies (e.g., Jeltsch-Thömmes et al., 2019), although there is not a consensus on the sign or magnitude of wind stress difference during the last glacial (Matsumoto et al., 2020).

Experiments LGM_Ice, LGM_Rad, LGM_Dust, LGM_Orbit, and LGM_Winds test the effects of each boundary condition applied on an individual basis to the modern equilibrium model state. Experiment LGM_Full was performed with all five boundary conditions applied together (Table 1). Each LGM experiment was run for 20,000 years, achieving steady state by the end of the model run. We performed a control run, LGM_Control, for the same duration of time under modern conditions. In each experiment and control run, excluding LGM_Rad and LGM_Full, atmospheric CO_2 was allowed to vary freely and to influence radiative feedback. In LGM_Rad

Paleoceanography and Paleoclimatology

10.1029/2022PA004522

Table 1
Summary of MESMO 3c Climate Forcing Experiments

							MOC			DOC			
			Air T	SST	pCO_2	Sea ice	Atl	SO	NPP	DOC_T	DOC_{SL}	DOC_R	DIC
Experiments	Description	Run ID	°C	°C	ppm	%	Sv	Sv	Pg C yr^{-1}	Pg C	Pg C	Pg C	Pg C
Glacial boundary conditions													
LGM_Control	Modern	220408b	13.6	18.5	279	10.5	12.4	41.7	34.6	675	27.3	648	37,335
LGM_Full	Full glacial	220408c	8.3	15.2	217	17.2	14.9	20.5	29.1	594	25.0	569	37,550
LGM_Ice	Glacial land ice	220408d	11.2	17.1	269	13.3	14.1	42.1	30.7	612	25.4	586	37,421
LGM_Rad	GHG = −2.6 W m-2	220408e	10.9	16.6	270	13.8	11.9	42.3	29.7	596	24.7	571	37,433
LGM_Dust	Glacial dust	220408f	13.8	18.6	248	10.4	12.3	41.6	40.5	783	32.0	751	37,301
LGM_Orbital	Glacial orbital	220408g	13.7	18.6	281	10.6	12.2	41.6	35.0	681	27.5	654	37,324
LGM_Winds	−50% SH westerlies	220408h	13.5	18.5	267	11.1	12.8	20.2	32.6	630	24.9	605	37,409
Freshwater hosing													
FH_Control	No hosing	220407v	13.6	18.5	279	10.5	12.4	41.7	34.6	676	27.3	648	37,335
FH_0.4	0.4 Sv hosing	220407w	14.7	19.3	315	8.5	1.0	41.2	41.6	711	33.2	677	37,222
FH_0.3	0.3 Sv hosing	220407x	14.7	19.3	313	8.5	1.2	41.2	41.2	707	32.8	674	37,229
FH_0.2	0.2 Sv hosing	220407y	14.6	19.2	310	8.7	1.7	41.3	40.1	699	31.8	668	37,243
FH_0.1	0.1 Sv hosing	220407z	14.0	18.8	288	9.7	5.5	41.5	36.0	680	28.4	652	37,310

Note. Physical and biogeochemical parameters were assessed at a point of steady state in the glacial boundary condition runs and control runs and at the final year of forced AMOC slowdown in all hosing experiments (model year 1050). MOC = meridional overturning circulation strength in the Atlantic and Southern Oceans, air T = global annual mean surface air temperature, SST = global annual mean sea temperature in the top 45 m, sea ice = global annual mean sea ice coverage, pCO_2 = partial pressure of atmospheric carbon dioxide, NPP = total annual community net primary production rate, DOC_T = global total DOC inventory, DOC_{SL} = global DOC_{SL} inventory, DOC_R = global DOC_R inventory, DIC = global total dissolved organic carbon inventory.

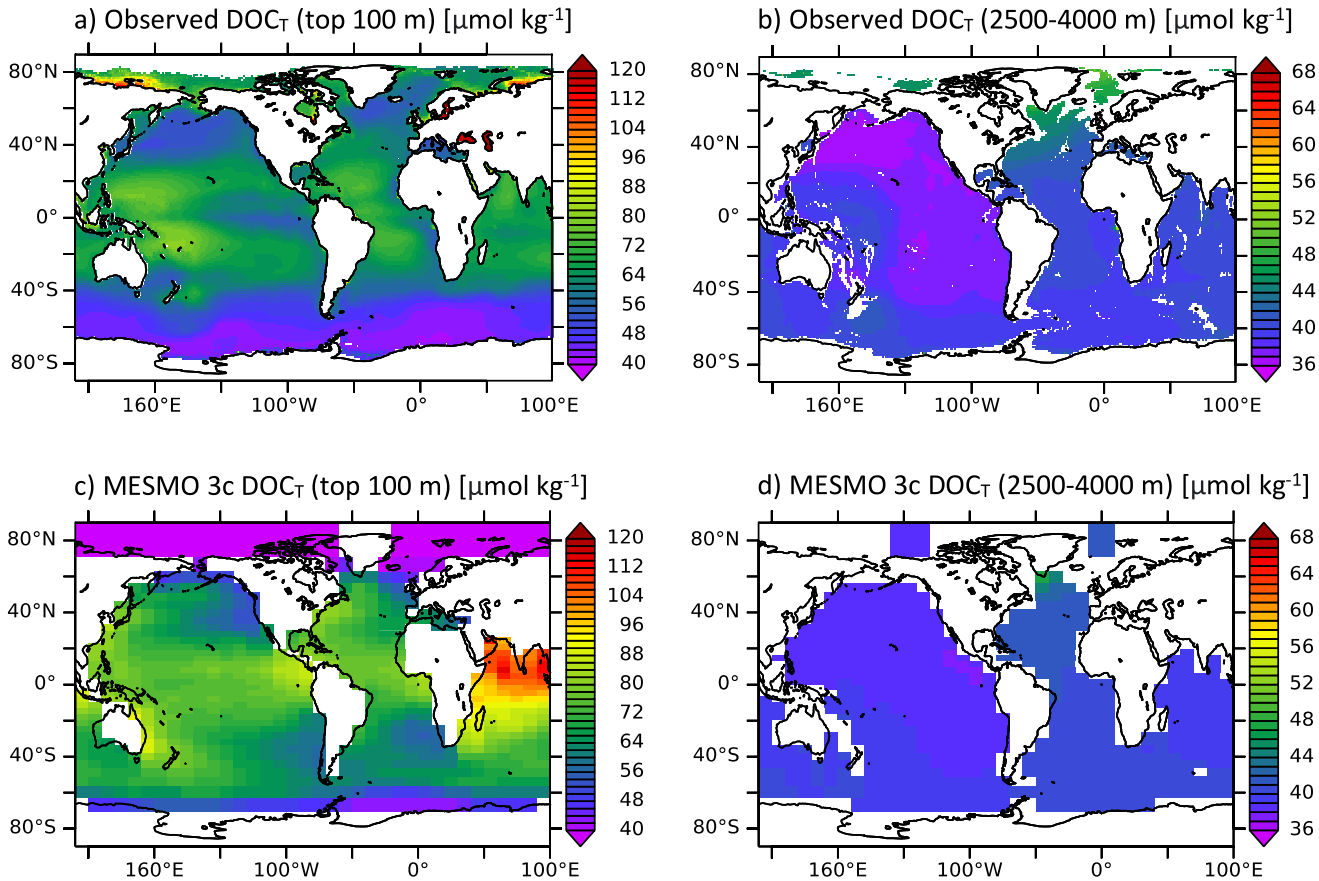

Figure 2. Comparison of surface and deep-ocean DOC_T distributions. (a, b) "Observed" DOC_T from Roshan and DeVries (2017), (c, d) MESMO 3c. See Figure S3 in Supporting Information S1 for a comparison between MESMO 3c and the previous model, MESMO 3.

and LGM_Full, atmospheric CO_2 was allowed to vary freely but not to influence radiative feedback, as a weaker radiative forcing was prescribed separately.

2.3.2. Freshwater Hosing

In the second set of experiments, we simulated AMOC weakening by introducing an influx of freshwater into the North Atlantic in the form of negative salinity perturbation to the grid boxes corresponding to this basin. The flux was applied for 1,000 years over the course of 2,500-year runs, starting at model year 50 and ending after model year 1050. A small, positive salinity flux was applied to the global ocean outside of the North Atlantic to maintain global salinity. Four experiments were performed in this manner, using freshwater forcing terms ranging from 0.1 to 0.4 Sv in order to trigger a range of AMOC responses (Table 1). These runs were initialized from the run equilibrated under modern conditions following Matsumoto and Yokoyama (2013). A control run, FH_Control, was performed for the 2,500 years under modern conditions with no freshwater forcing applied. In all experiments, atmospheric CO_2 was allowed to vary freely and to influence radiative feedback.

3. Results

The steady state distributions and inventories of DOC and related tracer properties from MESMO 3c under modern climate conditions are presented and compared to observationally-derived global DOC_T product (Roshan & DeVries, 2017) as well as to our previous versions of MESMO in Supporting Information S1 (Figures S2 and S3, Tables S1 and S3). In Figure 2, we compare just the horizontal DOC_T distribution at the surface and at depth. As elaborated in Supporting Information S1, MESMO 3c achieves maximum surface DOC_T concentrations of ~70–90 µmol kg^{-1} between latitudes ~30°S and ~30°N (except the Indian Ocean) and minimum concentrations of ~40 µmol kg^{-1} in the Southern Ocean. These are consistent with data-derived concentrations. In the Indian

Ocean, MESMO 3c overestimates the surface DOC_T concentrations, a problem also seen in comparable magnitude in another DOM model (Letscher et al., 2015). In the deep ocean, MESMO 3c achieves a gradient in DOC_T concentrations between the North Atlantic and North Pacific, with concentrations decreasing along the path of global deep water circulation as observed (~29% reduction, Hansell & Carlson, 1998).

3.1. Global DOC Reduction Under LGM Conditions

The response of MESMO 3c physics (e.g., atmospheric pCO_2, air temperature, sea ice cover, and overturning circulation strength) in LGM_Full and the individual glacial boundary condition experiments is summarized in Table 1. The physical responses are consistent with those reported by Matsumoto et al. (2020) for glacial climate simulations using MESMO 3.

Of the five boundary conditions, the glacial radiative forcing in LGM_Rad causes the greatest cooling in global mean sea surface temperature (SST) by 1.9°C, followed by a 1.4°C cooling by the glacial land ice boundary condition in LGM_Ice. The other boundary conditions do not cause any appreciable cooling. The cooling in the LGM_Rad and LGM_Ice experiments expands the global annual mean sea ice coverage from 10.5% in LGM_Control to 13.8% and 13.3%, respectively. The sea ice expansion and cooling lead to a reduction in the global NPP from 34.6 Pg C yr^{-1} in the control experiment to 29.7 and 30.7 Pg C yr^{-1} in LGM_Rad and LGM_Ice, respectively. As a consequence, the global ocean DOC_T inventory is reduced from 675 Pg C in the control to 596 and 612 Pg C in these experiments. At the same time, this cooling enhances the gas solubility and contributes to a drawdown of atmospheric pCO_2 by approximately 10 ppm in both experiments (Table 1).

A precise quantitative attribution of the 10 ppm drop in LGM_Rad and LGM_Ice to the various drivers of pCO_2 is not possible in a dynamical model such as MESMO 3c, because changes in SST, stratification, circulation, sea ice, and biological production occur at the same time. However, a process of elimination suggests that gas solubility is likely the dominant driver. For example, the 10 ppm drop cannot be explained by the simulated reductions in DOC_T inventory or export production, both of which would predict a higher pCO_2. Similarly, AMOC changes in the opposite directions in the two experiments. The fact that the 10 ppm reduction predicted by MESMO 3c with DOC_R enabled in this study is smaller than the 15–20 ppm drop predicted by MESMO 3 without DOC_R in the equivalent experiments (Matsumoto et al., 2020) points to the role that DOC_R played in moderating the drop in atmospheric pCO_2 in these experiments. Rather, the reduced pCO_2 in LGM_Rad and LGM_Ice can only be explained by the increased global DIC inventory (Table 1). Increased solubility, the remaining pCO_2 driver, is thus likely the dominant driver of the DIC increase and thus the pCO_2 drop.

As described previously (Matsumoto et al., 2020), glacial dust in LGM_Dust triggers a cascade of large changes in biological production, even while the model physics is nearly the same in LGM_Dust and LGM_Control (Table 1, Table S4 in Supporting Information S1). Overall, the global NPP in LGM_Dust jumps by 17% from 34.6 Pg C in the control run to 40.5 Pg C yr^{-1}. The global export production increases from 9.8 to 11.6 Pg C yr^{-1}. These production increases in the model are driven by a net increase in eukaryotes at the expense of cyanobacteria (Table S4 in Supporting Information S1). This enhanced growth of eukaryotes, which include diatoms, occurs in the lower latitudes in a manner predicted by the Silicic Acid Leakage Hypothesis (SALH) (Brzezinski et al., 2002; Matsumoto et al., 2002). In this hypothesis, Fe input into the glacial Southern Ocean reduces the Si:N uptake ratio by Antarctic diatoms, forming a pool of underutilized Si in the Southern Ocean that escapes its trapping there and leaks out to the lower latitudes via Antarctic Intermediate Water and Antarctic Mode Water. Consistent with these SALH predictions, the global ocean surface silicic acid concentration in LGM_Dust more than doubles, relieves the Si limitation on eukaryotes, and boosts their production from 31% of global NPP in the control to 57% in LGM_Dust (Table S4 in Supporting Information S1). Eukaryotes are opportunistic phytoplankton, which is reflected in the model by high growth rates. The enhanced growth of eukaryotes strongly depletes phosphate in surface waters, thereby limiting the relative growth of the other two PFTs in the model, cyanobacteria and diazotrophs. The overall larger production in LGM_Dust has two important carbon cycle consequences: 31 ppm lower atmospheric pCO_2 and 108 Pg C higher global ocean DOC_T inventory (Table 1). The lower pCO_2 in this experiment is entirely driven by DOC_T because the global ocean DIC pool shrunk by 34 Pg C.

The boundary condition experiment LGM_Winds is potentially interesting in that it sheds some light on the Shen and Benner (2018) prediction, which posits that a weakening of the global overturning circulation should ultimately lead to a larger global ocean DOC_T inventory. In the LGM_Winds experiment, the Southern Ocean

overturning circulation is indeed weakened by approximately half, from 41.7 Sv (Sv = 10^6 m^3 s^{-1}) to 20.2 Sv (Table 1), yet the global DOC_T inventory does not increase as predicted but decreases by 45 Pg C. In this experiment, there is no change in the global mean SST or AMOC, but the Southern Ocean MLD shoals by 130 m from 426 m, and there are reductions in the global NPP by 2 Pg C yr^{-1} and atmospheric pCO_2 by 12 ppm compared to LGM_Control (Table 1). These changes apparently compensate for the effect that DOC_T removal mechanism envisioned by Shen and Benner (2018) have on DOC_T removal under weakened overturning circulation. It is also worth noting that in the LGM_Winds experiment, the 12 ppm reduction in atmospheric pCO_2 cannot be explained by a reduction in DOC_T inventory but by an increase in the global DIC inventory by 74 Pg C (Table 1).

The combination of all the glacial boundary conditions in LGM_Full brings about a polar sea ice coverage expansion to 17.2% of the global ocean, a slightly more vigorous AMOC and much reduced Southern Ocean overturning, a global SST cooling by 3.3°C, a drop in atmospheric pCO_2 drops by 62 ppm, a reduced global NPP by 5.5 Pg C yr^{-1}, a larger global DIC inventory by 215 Pg C, and a smaller global DOC_T inventory by 81 Pg C compared to LGM_Control (Table 1). Even while global NPP is reduced by 5.5 Pg C yr^{-1}, which represents a 34% drop, the global export production is reduced by only 2% from 9.8 to 9.6 Pg C yr^{-1} (Table S4 in Supporting Information S1). This is due to the lower temperatures in the experiment raising fPOM according to Equation 1 and to the elevated C:P stoichiometry of export production (Matsumoto et al., 2020). The C:P ratio increases from 106:1 in LGM_Control to 136:1 in LGM_Full.

In LGM_Full, the lower NPP and higher fPOM both contribute to reduced DOM production rates and a DOC_T inventory that is smaller by 81 Pg C, which would tend to raise atmospheric pCO_2 by 38 ppm. DOC_R inventory change of 79 Pg C accounts for much of this DOC_T change (Table 1). These changes are accompanied by spatial reorganization of DOC_T concentrations (Figures 3a and 3b). Production layer (top 100 m) DOC_T concentrations decrease in most regions, with the greatest reductions occurring in the Southern and Indian Oceans (>20 μmol kg^{-1} reduction), followed by the north Pacific and the Pacific and Atlantic subtropics. DOC_T concentrations increase modestly by up to 10 μmol kg^{-1} in the western equatorial Pacific and nominally in the North Atlantic (Figure 3b).

The first order pattern of surface DOC_T concentrations is expected to be determined by NPP, fPOM, and DOC photodegradation rates. Despite the temperature dependence in the formulation of all these factors in MESMO 3c, there is little spatial coherence between changes in SST and changes in DOC_T spatial distribution in LGM_Full versus LGM_Control (Figures 3b and 3c). SST under the full glacial conditions decreased globally, as expected, with the strongest reductions occurring in the subpolar Atlantic and Pacific Oceans. We note that the further poleward regions are covered by ice under full LGM conditions, and that the seawater freezing point of ∼2°C imposes a limit on SST reduction in these regions.

The changes in surface DOC_T in LGM_Full are much more coherent with NPP changes than with SST changes (Figures 3b and 3d). The pattern of NPP changes is unlike that of SST changes because temperature is but one driver of NPP. Other drivers of NPP are nutrients, MLD, and light. In the case of LGM_Full, the nutrient control is important because the cascade of biological impacts that are triggered by the Fe input in LGM_Dust occur in LGM_Full as well. It is important to note that the spatial pattern of total NPP changes (Figure 3d) is given by the sum of the NPP changes of the individual PFTs (Figure S4 in Supporting Information S1), pointing to the importance of taxonomy in fully understanding NPP changes.

The simulated DOC_T production rate changes are spatially coherent with removal rate changes in the surface ocean (Figures 3e and 3f). Again, neither resemble SST changes but rather NPP changes. These comparisons suggest that NPP, which depends on several variables other than temperature, is an overarching control on both DOC production and degradation rate changes in the LGM boundary condition experiments. The signs of NPP change (increase or decrease), along with the signs of DOC_{SL} and DOC_R change, are consistent with the sign of DOC_T change across all five of these experiments (Table 1).

3.2. Global DOC Increase Under Weakened AMOC State

In every freshwater hosing experiment, AMOC weakening produces the expected spatial response in SST: cooling in the North Atlantic—where freshwater was applied—and warming in the South Atlantic, typical of the well-observed antiphased, "bipolar seesaw" between the hemispheres (Crowley, 1992). The transient AMOC weakening is associated with warming in the global surface ocean (as well as global surface air, not shown) and higher atmospheric pCO_2 during the time of active hosing perturbation (Figures 4a–4c). These changes are

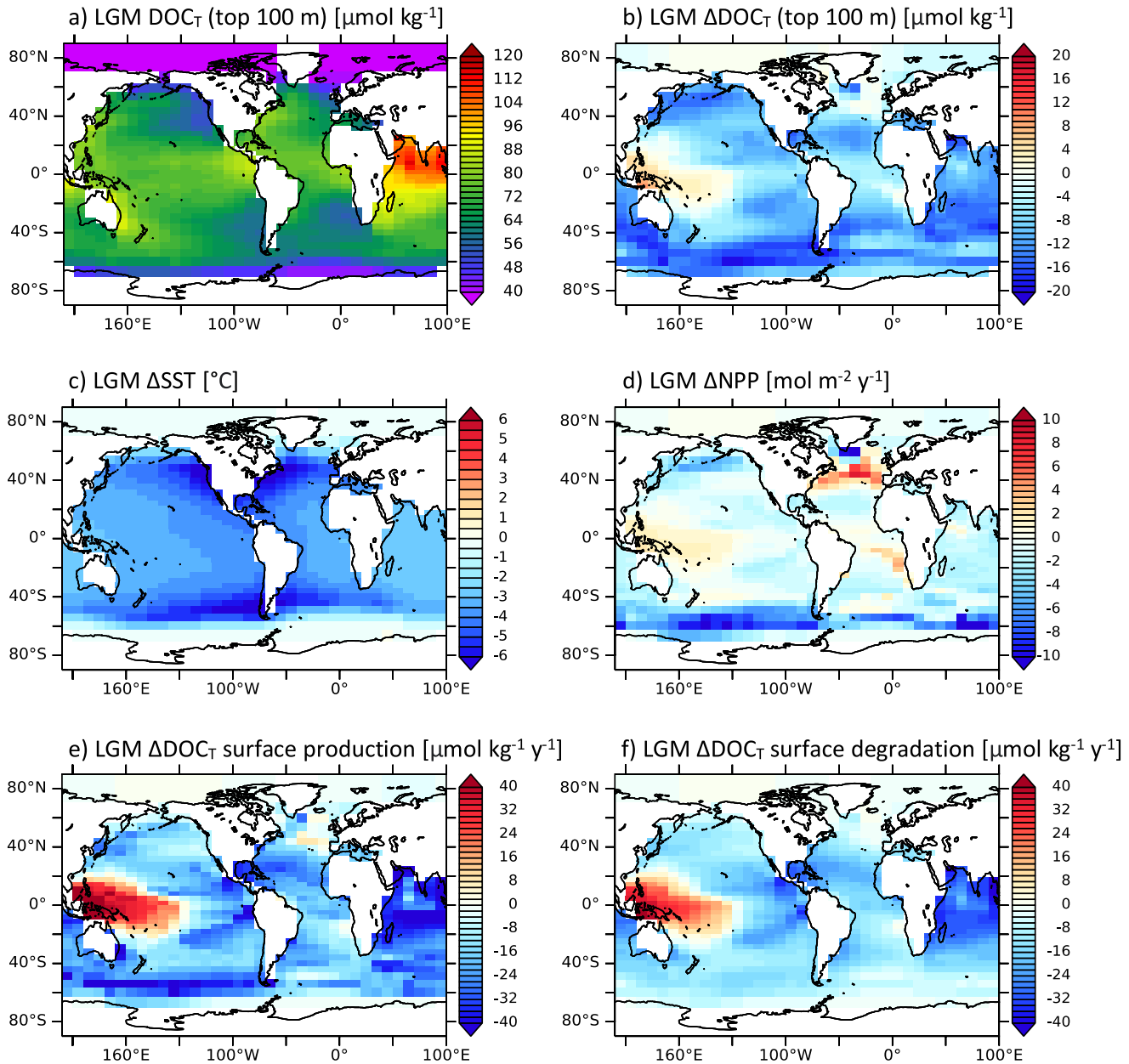

Figure 3. Assessment of DOC_T and potential driving factors under full LGM boundary conditions. (a) DOC_T in top 100 m, (b) ΔDOC_T (LGM_Full—LGM_Control) in top 100 m, (c) ΔSST (LGM_Full—LGM_Control), (d) ΔNPP (LGM_Full—LGM_Control) in top 100 m, (e) ΔDOC_T surface production rate (LGM_Full—LGM_Control), (f) ΔDOC_T surface degradation rate (LGM_Full—LGM_Control).

accompanied by increases in global DOC_T, DOC_R, and DOC_{SL} inventories (Table 1). The simulated changes are qualitatively similar across all experiments but are greater for larger freshwater perturbations. For example, during maximum AMOC weakening in year 1050, DOC_T inventory is increased by 35 Pg C (5.2%) in FH_0.4 in comparison to just 5 Pg C (0.7%) in FH_0.1 (Table 1). We do not show the same set of hosing experiments carried out under glacial conditions because the results are qualitatively the same, and we are interested in examining the DOC_T inventory response to a different set of climate change conditions.

In Figures 4d–4h, we illustrate the representative, modeled biogeochemical response from FH_0.4, as 0.4 Sv hosing produced an atmospheric pCO_2 response (+36 ppm) comparable to that of deglacial stadial HS1 (Bauska et al., 2016; Table 1) as well as reasonable Greenland air temperature and SST anomalies for this event (He et al., 2021; Figure S5 in Supporting Information S1).

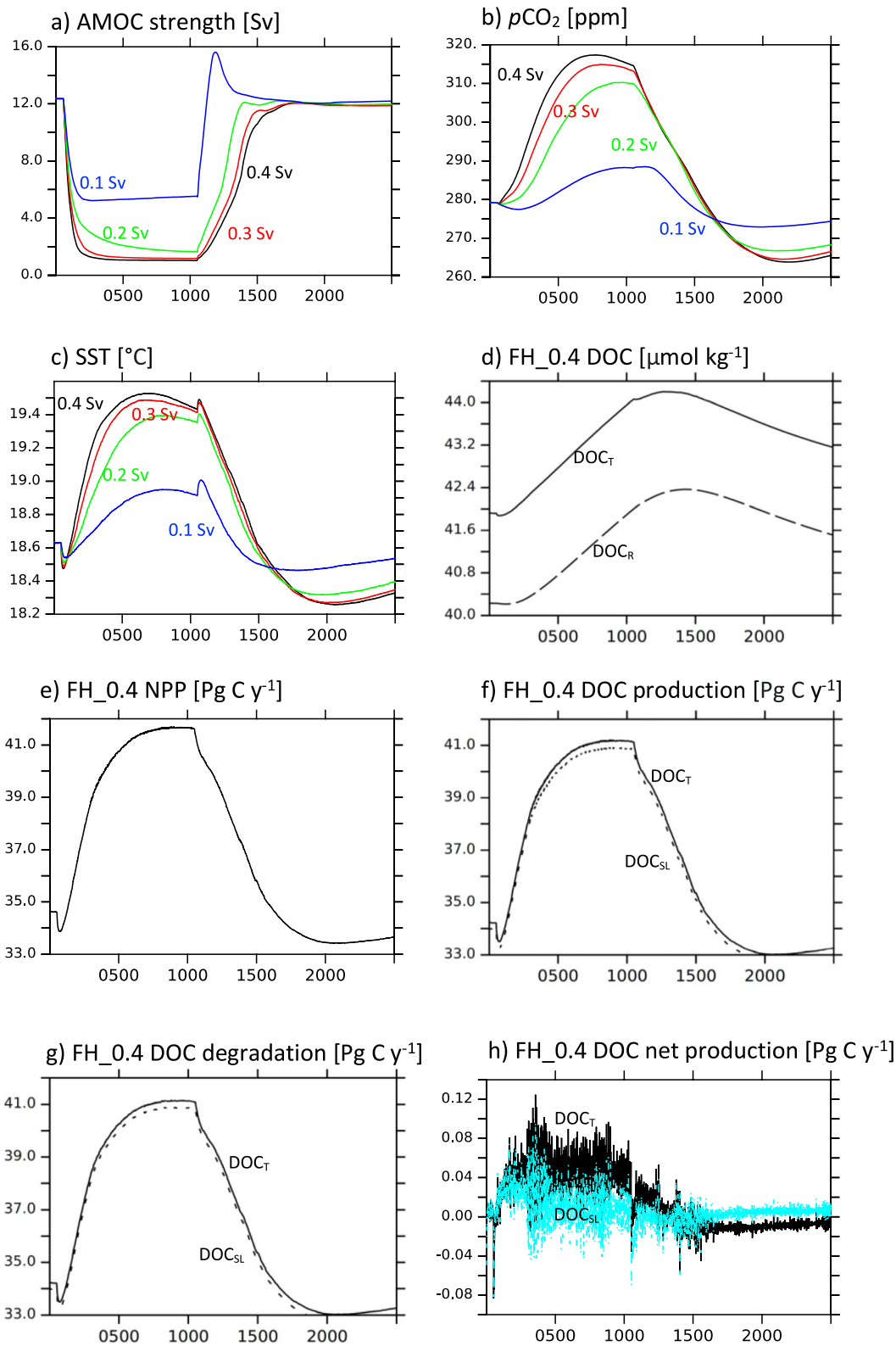

Figure 4. Response of MESMO 3c to variable magnitudes of freshwater forcing (a)–(c) and 0.4 Sv freshwater hosing (d)–(h). (a) AMOC strength (Sv), (b) atmospheric pCO_2 (ppm), (c) global average SST (°C), (d) global average DOC_T (solid line) and DOC_R (dashed line) concentrations (µmol kg^{-1}), (e) global NPP (Pg C y^{-1}), (f) global DOC_T (solid line) and DOC_{SL} (dotted line) production rates (Pg C y^{-1}), (g) global DOC_T (solid line) and DOC_{SL} (dotted line) degradation rates (Pg C y^{-1}), (h) global production rate minus degradation rates for DOC_T (black solid line) and DOC_{SL} (light blue dashed line) (Pg C y^{-1}). Horizontal axis = time in years.

In the FH_0.4 experiment, NPP and the total global production and degradation rates of DOC increase over the course of the weakened AMOC state (Figures 4f and 4g). However, the production rate increases to a greater extent than the degradation rate, resulting in net DOC accumulation (Figure 4h). Also, there is a clear spatial coherence between changes in production layer DOC_T, SST, and NPP relative to the control at model year 1050 (again shown only for FH_0.4 in Figure S4 in Supporting Information S1).

4. Discussion

In this study, MESMO 3c is not coupled to the sediment module and is thus a closed system with regards to the atmosphere-ocean carbon. Since carbon is conserved in the system, any changes in atmospheric carbon must be accounted for by ocean storage changes in the opposite sense but of equal magnitude. All of our sensitivity experiments allowed atmospheric pCO_2 to vary freely in response to the prescribed boundary conditions. Whereas past modeling studies have traditionally equated the total ocean storage to the global ocean DIC inventory, the storage in MESMO 3c is given here by the sum of the global ocean DOC_T and DIC inventories. Thus, in our experiments, the change in atmospheric pCO_2 is not quantitatively consistent with the change in the DIC inventory alone (Table 1). For example, atmospheric pCO_2 decreased and DIC inventory increased in LGM_Full, LGM_Ice, and LGM_Rad, but the DIC increase was either too great or too small to fully explain the atmospheric pCO_2 reduction. In LGM_Full, for example, atmospheric pCO_2 was reduced overall by 62 ppm, which is the result of the 215 Pg C larger DIC pool lowering pCO_2 and the 81 Pg C smaller DOC_T pool raising pCO_2. In the case of LGM_Dust, both atmospheric pCO_2 and DIC inventory decreased, so the even the sign of DIC change was inconsistent with the pCO_2 change.

Our results demonstrate clearly that DIC alone cannot fully explain the difference in atmospheric CO_2 storage between the preindustrial and glacial climate states in MESMO 3c, in which the marine DOC pool is similar in size to the atmospheric carbon pool, as per observations. Across the full LGM and glacial boundary condition runs, the difference in DIC between preindustrial and glacial explains 37% of the variability in CO_2 difference between these two states (blue triangles, Figure 5a). DOC difference alone does not explain any variability (green circles). However, the sum of DIC and DOC difference lies on a −1:1 line and can account for >99% of the variability in CO_2 difference between the preindustrial and glacial states (orange diamonds). The importance of the DOC pool in fully accounting for atmospheric pCO_2 under glacial conditions has previously been pointed out by Ma and Tian (2014). However, in their DOC modeling work using the GENIE model, DOC degradation was determined simply by uniform degradation timescales without any environmental dependence, and the DOC production decreased due to cooling and salinity-induced stratification.

We find that the importance of dynamic DOC in accounting for atmospheric CO_2 under glacial conditions is equally true under a very different climate state of freshwater-induced AMOC weakening. Again, DIC alone is unable to quantitatively explain the simulated changes in atmospheric CO_2 (blue triangles are off the −1:1 line, Figure 5b), although the global DIC inventory changes consistently in the correct sense and has a high predictive power ($R^2 > 99\%$). Across the hosing experiments, atmospheric pCO_2 increases and DIC inventory is reduced; however, the DIC reduction is too large for it alone to quantitatively account for pCO_2. In these experiments, there is a consistent increase in the global ocean DOC_T inventory with AMOC weakening that counters the DIC inventory change (green circles, Figure 5b; Table 1). In fact, the high level of consistency also gives DOC a high predictive power for pCO_2 in these experiments ($r^2 > 96\%$). However, it is the sum of DOC and DIC inventories that can quantitatively account for atmospheric CO_2 changes across all freshwater hosing experiments (orange diamonds lie on the −1:1 line, Figure 5b).

While the total DIC content of the ocean exceeds the DOC content by two orders of magnitude, in many experiments, DOC_T inventory changes by the same order or even greater than the magnitude of DIC changes. For example, in the glacial experiment LGM_Dust, $\Delta DOC_T = 108$ Pg C while $\Delta DIC = -34$ Pg C (Table 1). That the response of the DOC reservoir to the climate changes simulated by our experiments is disproportionate to its relative size implies that its mobility may be significant in the context of global climate on centennial and millennial timescales.

This implication raises the question of controls on marine DOC dynamics. As noted above, the literature suggests two possible controls: (a) the temperature hypothesis (Lønborg et al., 2018), which proposes that a warmer ocean would increase temperature-dependent DOC degradation rates and reduce the total inventory, implying the opposite for a colder ocean; and (b) the circulation hypothesis (Shen & Benner, 2018), which proposes that a reduction in global overturning circulation would decrease exposure of DOC to surface degradation processes, leading to

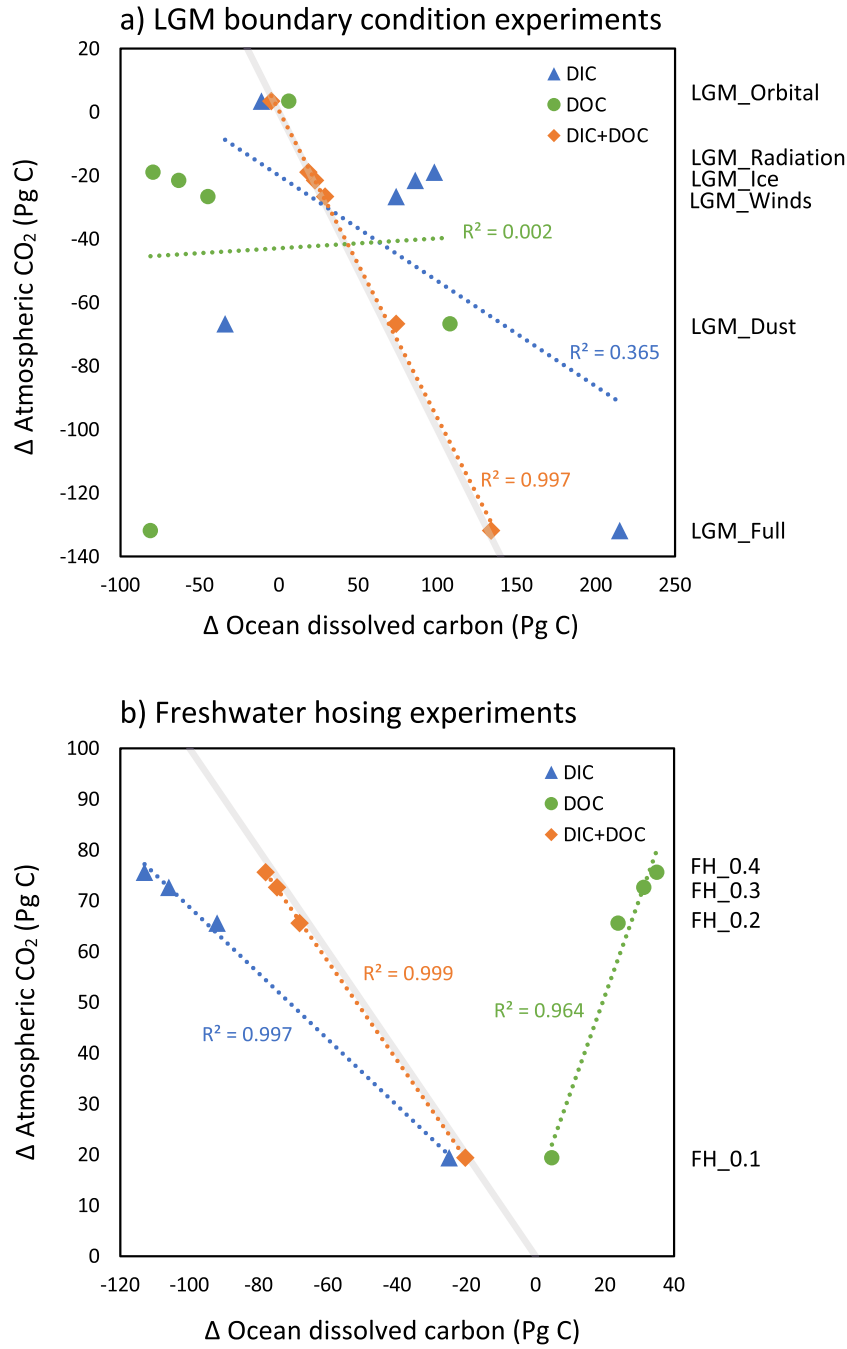

Figure 5. Change in dissolved ocean carbon pools versus change in atmospheric CO_2 relative to control in (a) LGM boundary condition experiments and (b) freshwater hosing experiments at year 1050. Blue = ΔDIC, green = ΔDOC, orange = Δ(DIC + DOC). The dotted lines are the linear regression fit for each parameter. The gray line is the −1:1 line. Atmospheric CO_2 [Pg C] = atmospheric pCO_2 [ppm] × 2.13. Δ = experiment-control.

accumulation in the interior ocean and increasing the total DOC inventory. Both hypotheses rely on removal rate as the driving factor. The introduction of temperature-dependent DOC removal processes in MESMO 3c, coupled with a refinement of the environmentally-dependent DOC production mechanism, allowed us to examine these dynamics.

Our modeling results indicate that changes in DOC inventory (Table 1) are predominantly controlled by changes in production rate (Figures 3 and 4) rather than in removal rate. We find that in both sets of experiments, changes

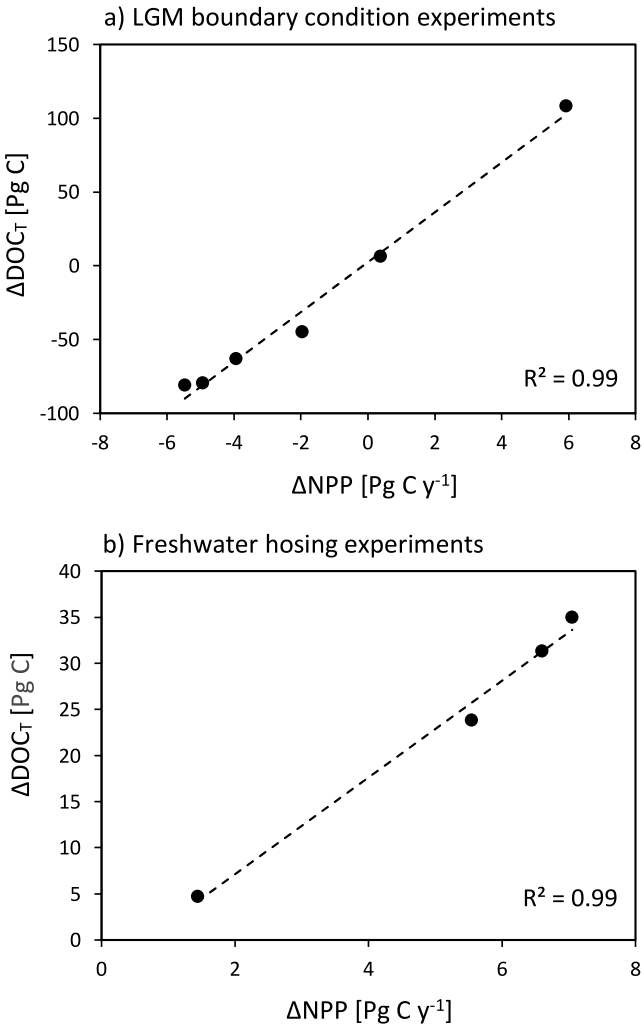

Figure 6. Difference from control in global NPP versus difference from control in DOC_T inventory in all (a) Last Glacial Maximum (LGM) boundary conditions experiments and (b) freshwater hosing experiments at year 1050. NPP and DOC_T were assessed at steady state in the LGM boundary condition experiments and during the last year of forced AMOC slowdown in the hosing experiments. Δ = experiment-control.

in DOC production respond by a greater magnitude than do changes in DOC degradation. Because of the temperature dependence of DOC degradation in MESMO 3c (microbial degradation of DOC_{SL} and photodegradation of DOC_R), global cooling in the model induces lower global DOC degradation rates, and global warming induces faster global degradation rates. These changes are driven primarily by changes in DOC_{SL} degradation rate (e.g., Figure 4g), although photodegradation is the primary driver of changes to DOC_R degradation rate, as it is the only temperature-dependent DOC_R removal mechanism and occurs on timescales two to three orders of magnitude faster than background removal. However, changes in global DOC production rates are comparatively greater and ultimately cause changes in the DOC_T, DOC_{SL}, and DOC_R inventories in the same sense (Table 1). For example, linear regression analyses indicate that changes in NPP explain the changes in DOC_T inventory size with $R^2 = 0.99$ in both the LGM and freshwater hosing experiments (Figure 6).

In the freshwater forcing experiments, AMOC weakening triggers a regional cooling in the North Atlantic region, but warming elsewhere, so that there is warming globally (Figure S4 in Supporting Information S1). Thus, the globally integrated degradation rates for both DOC pools increases over the course of AMOC slowdown. Another factor that may contribute to increased degradation rates in our model is that a weakened AMOC has likely lengthened the residence time of surface water, so that DOC_R is subject to photodegradation for a longer time. Because the elevated production rates outpace the increases in degradation rates, global mean DOC concentrations and total inventories increase despite the higher global DOC degradation rates (Figure 4). Again, this result points to the importance of DOC production in controlling the global DOC inventory.

This set of freshwater hosing experiments further allowed us to evaluate the circulation mechanism. According to Shen and Benner (2018), AMOC weakening should reduce DOC exposure to degradation mechanisms, which is inconsistent with our result of increased DOC degradation rates (Figure 4). They were concerned with ocean circulation transporting DOC_R to various ocean environments—such as coastal areas—where DOC_R could be broken down by specialized microbes, which are not prevalent in the deep ocean. They did not consider changes in temperature or residence time that would be integral to global climate change that could also affect DOC degradation.

Similarly, the results from the glacial boundary condition experiment LGM_Winds do not support the Shen and Benner (2018) prediction. In this experiment, the Southern Ocean overturning circulation becomes weaker by half while global SST and AMOC do not change much. At the same time, there is a reduction in global NPP by 2 Pg C yr^{-1} and global DOC_T inventory by 45 Pg C (Table 1). In contrast to the Shen and Benner (2018) prediction, a weaker overturning circulation leads to a smaller global ocean DOC pool in our model.

The hypotheses of Lønborg et al. (2018) and Shen and Benner (2018) both focus on one DOC degradation mechanism, the effect of either ocean temperature or circulation, in the absence of any other changes. Our study reveals that such an assumption does not hold in a dynamical system. Other important drivers of DOC dynamics include light availability (via MLD) and internal nutrient cycling (via stratification and circulation), which both affect DOC production. Under climate change, these drivers can change along with the drivers identified by the two hypotheses. In the case of glacial climate, even the external supply of micronutrient Fe can change, which can trigger a cascade of substantial biogeochemical changes with implications for DOC dynamics.

5. Conclusions

The marine DOC reservoir rivals atmospheric carbon inventory in size and has been implicated in past climate change events; however, its dynamics on geologic timescales have not been explicitly studied. In this study, we used an EMIC with novel features to represent the marine DOC cycle, including temperature-dependent DOC production and degradation. Our model simulation results indicate that DOC inventory, most of which is refractory DOC, is responsive to climate forcings with net change in DOC inventory generally controlled by production changes rather than degradation changes. Under conditions representative of the LGM, the marine DOC inventory was reduced by nearly 100 Pg C relative to preindustrial, and collapse of the AMOC had the potential to increase marine DOC by up to 35 Pg C. Furthermore, our work highlights the importance of DOC in accounting for changes in atmospheric CO_2 during changing climate events. In a closed atmosphere-ocean system, atmospheric CO_2 change should be inversely related to total ocean carbon inventory through mass conservation. Our results indicate clearly that the total ocean carbon inventory is accurately represented by the sum of the marine DIC and DOC reservoirs, rather than simply DIC as has traditionally been assumed by the paleoclimate community. Depending on the climate change scenario, DOC changes can either enhance or diminish the effect that DIC has on atmospheric CO_2. In other words, just considering DIC would lead to over- or under-estimation of atmospheric CO_2 change. Consideration of DOC is thus critical in improving our understanding of the connection between ocean carbon cycling processes and global climate over geologic timescales. A credible representation of refractory DOC and its production in models is critical for fully understanding the ∼100 ppm glacial CO_2 drawdown, and more broadly, the global carbon cycle and climate of the past. At the same time, there is room to improve DOC modeling that would enhance the significance of model implications. For example, the current literature describing theory and observations of how temperature affects DOC degradation is limited. Additionally, environmental controls on NPP partitioning into the particle and dissolved pools are not well understood. We believe that improvements in such formulations will enhance the fidelity of the results of DOC modeling with respect to paleoclimatology.

Data Availability Statement

Code for MESMO 3c is available from Zenodo (Gilchrist & Matsumoto, 2023). Model results have been archived with the Biological & Chemical Oceanography Data Management Office (BCO-DMO) and are available freely (Matsumoto & Gilchrist, 2022).

Acknowledgments
This work was supported by the U.S. National Science Foundation (OCE-1827948). Numerical modeling and analysis were carried out using resources at the University of Minnesota Supercomputing Institute.

References

Anderson, R. F., Ali, S., Bradtmiller, L. I., Nielsen, S. H. H., Fleisher, M. Q., Anderson, B. E., & Burckle, L. H. (2009). Wind-driven upwelling in the Southern Ocean and the deglacial rise in atmospheric CO_2. *Science*, *323*(5920), 1443–1448. https://doi.org/10.1126/science.1167441

Archer, D., Eby, M., Brovkin, V., Ridgwell, A., Cao, L., Mikolajewicz, U., et al. (2009). Atmospheric lifetime of fossil fuel carbon dioxide. *Annual Review of Earth and Planetary Sciences*, *37*(1), 117–134. https://doi.org/10.1146/annurev.earth.031208.100206

Arrieta, J. M., Mayol, E., Hansman, R. L., Herndl, G. J., Dittmar, T., & Duarte, C. M. (2015). Ocean chemistry: Dilution limits dissolved organic carbon utilization in the deep ocean. *Science*, *348*(6232), 331–333. https://doi.org/10.1126/science.1258955

Bauska, T. K., Baggenstos, D., Brook, E. J., Mix, A. C., Marcott, S. A., Petrenko, V. V., et al. (2016). Carbon isotopes characterize rapid changes in atmospheric carbon dioxide during the last deglaciation. *Proceedings of the National Academy of Sciences of the United States of America*, *113*(13), 3465–3470. https://doi.org/10.1073/pnas.1513868113

Benner, R., & Amon, R. M. W. (2015). The size-reactivity continuum of major bioelements in the ocean. *Annual Review of Marine Science*, *7*(1), 185–205. https://doi.org/10.1146/annurev-marine-010213-135126

Bereiter, B., Eggleston, S., Schmitt, J., Nehrbass-Ahles, C., Stocker, T. F., Fischer, H., et al. (2015). Revision of the EPICA Dome C CO_2 record from 800 to 600 kyr before present. *Geophysical Research Letters*, *42*(2), 542–549. https://doi.org/10.1002/2014GL061957

Berger, A. L. (1978). Long-term variations of daily insolation and quaternary climate changes. *Journal of the Atmospheric Sciences*, *35*(12), 2362–2367. https://doi.org/10.1175/1520-0469(1978)035<2362:LTVODI>2.0.CO;2

Bond, G., Heinrich, H., Broecker, W., Labeyrie, L., McManus, J., Andrews, J., et al. (1992). Evidence for massive discharges of icebergs into the North Atlantic ocean during the last glacial period. *Nature*, *360*(6401), 245–249. https://doi.org/10.1038/360245a0

Broecker, W. S., & Peng, T. H. (1982). *Tracers in the sea* (pp. 1–690). Eldigio Press.

Brzezinski, M. A., Pride, C. J., Franck, V. M., Sigman, D. M., Sarmiento, J. L., Matsumoto, K., et al. (2002). A switch from $Si(OH)_4$ to NO_3^- depletion in the glacial Southern Ocean. *Geophysical Research Letters*, *29*(12), 1564. https://doi.org/10.1029/2001GL014349

Carlson, C. A., Giovannoni, S. J., Hansell, D. A., Goldberg, S. J., Parsons, R., & Vergin, K. (2004). Interactions among dissolved organic carbon, microbial processes, and community structure in the mesopelagic zone of the northwestern Sargasso Sea. *Limnology & Oceanography*, *49*(4), 1073–1083. https://doi.org/10.4319/lo.2004.49.4.1073

Crowley, T. J. (1992). North Atlantic deep water cools the southern hemisphere. *Paleoceanography*, *7*(4), 489–497. https://doi.org/10.1029/92PA01058

Dunne, J. P., Armstrong, R. A., Gnnadesikan, A., & Sarmiento, J. L. (2005). Empirical and mechanistic models for the particle export ratio. *Global Biogeochemical Cycles*, *19*, 1–16. https://doi.org/10.1029/2004GB002390

Eppley, R. (1972). Temperature and phytoplankton growth in the sea. *Fisheries Bulletin*, *70*, 1063–1085.
Follett, C. L., Repeta, D. J., Rothman, D. H., Xu, L., & Santinelli, C. (2014). Hidden cycle of dissolved organic carbon in the deep ocean. *Proceedings of the National Academy of Sciences of the United States of America*, *111*(47), 16706–16711. https://doi.org/10.1073/pnas.1407445111
Gilchrist, M., & Matsumoto, K. (2023). gaia3intc/mesmo: MESMO v3.0c features calibrated and environmentally dependent DOM (v3.0c) [Software]. Zenodo. https://doi.org/10.5281/ZENODO.7672202
Hansell, D. A. (2013). Recalcitrant dissolved organic carbon fractions. *Annual Review of Marine Science*, *5*(1), 421–445. https://doi.org/10.1146/annurev-marine-120710-100757
Hansell, D. A., & Carlson, C. A. (1998). Deep ocean gradients in dissolved organic carbon concentrations. *Nature*, *395*(6699), 263–266. https://doi.org/10.1038/26200
Hansell, D. A., Carlson, C. A., Repeta, D. J., & Schlitzer, R. (2009). Dissolved organic matter in the ocean: A controversy stimulates new insights. *Oceanography*, *22*(4), 202–211. https://doi.org/10.5670/oceanog.2009.109
He, C., Liu, Z., Otto-Bliesner, B. L., Brady, E. C., Zhu, C., Tomas, R., et al. (2021). Abrupt Heinrich Stadial 1 cooling missing in Greenland oxygen isotopes. *Science Advances*, *7*(25), 1–10. https://doi.org/10.1126/sciadv.abh1007
Jahn, A., Lindsay, K., Giraud, X., Gruber, N., Liu, Z., & Brady, E. C. (2015). Carbon isotopes in the ocean model of the community Earth system model (CESM1). *Geoscientific Model Development*, *8*, 2419–2434. https://doi.org/10.5194/gmd-8-2419-2015
Jeltsch-Thömmes, A., Battaglia, G., Cartapanis, O., Jaccard, S. L., & Joos, F. (2019). Low terrestrial carbon storage at the Last Glacial Maximum: Constraints from multi-proxy data. *Climate of the Past*, *15*(2), 849–879. https://doi.org/10.5194/cp-15-849-2019
Joos, F., Roth, R., Fuglestvedt, J. S., Peters, G. P., Enting, I. G., von Bloh, W., et al. (2013). Carbon dioxide and climate impulse response functions for the computation of greenhouse gas metrics: A multi-model analysis. *Atmospheric Chemistry and Physics*, *13*(5), 2793–2825. https://doi.org/10.5194/acp-13-2793-2013
Joos, F., & Spahni, R. (2008). Rates of change in natural and anthropogenic radiative forcing over the past 20,000 years. *Proceedings of the National Academy of Sciences of the United States of America*, *105*(5), 1425–1430. https://doi.org/10.1073/pnas.0707386105
Lang, S. Q., Butterfield, D. A., Lilley, M. D., Paul Johnson, H., & Hedges, J. I. (2006). Dissolved organic carbon in ridge-axis and ridge-flank hydrothermal systems. *Geochimica et Cosmochimica Acta*, *70*(15), 3830–3842. https://doi.org/10.1016/j.gca.2006.04.031
Laufkötter, C., John, J. G., Stock, C. A., & Dunne, J. P. (2017). Temperature and oxygen dependence of the remineralization of organic matter. *Global Biogeochemical Cycles*, *31*(7), 1038–1050. https://doi.org/10.1002/2017GB005643
Laws, E. A., Falkowski, P. G., Smith, W. O., Ducklow, H., & McCarthy, J. J. (2000). Temperature effects on export production in the open ocean. *Global Biogeochemical Cycles*, *14*(4), 1231–1246. https://doi.org/10.1029/1999GB001229
Letscher, R. T., & Moore, J. K. (2015). Preferential remineralization of dissolved organic phosphorus and non-Redfield DOM dynamics in the global ocean: Impacts on marine productivity, nitrogen fixation, and carbon export. *Global Biogeochemical Cycles*, *29*(3), 325–340. https://doi.org/10.1002/2014GB004904
Letscher, R. T., Moore, J. K., Teng, Y. C., & Primeau, F. (2015). Variable C: N: P stoichiometry of dissolved organic matter cycling in the community Earth system model. *Biogeosciences*, *12*(1), 209–221. https://doi.org/10.5194/bg-12-209-2015
Lønborg, C., Alvarez-Salgado, X. A., Letscher, R. T., & Hansell, D. A. (2018). Large stimulation of recalcitrant dissolved organic carbon degradation by increasing ocean temperatures. *Frontiers in Marine Science*, *4*, 1–11. https://doi.org/10.3389/fmars.2017.00436
López-Urrutia, A., San Martin, E., Harris, R. P., & Irigoien, X. (2006). Scaling the metabolic balance of the oceans. *Proceedings of the National Academy of Sciences of the United States of America*, *103*(23), 8739–8744. https://doi.org/10.1073/pnas.0601137103
Ma, W., & Tian, J. (2014). Modeling the contribution of dissolved organic carbon to carbon sequestration during the last glacial maximum. *Geo-Marine Letters*, *34*(5), 471–482. https://doi.org/10.1007/s00367-014-0378-y
Ma, W., Wang, P., & Tian, J. (2017). Modeling 400–500-kyr Pleistocene carbon isotope cyclicity through variations in the dissolved organic carbon pool. *Global and Planetary Change*, *152*, 187–198. https://doi.org/10.1016/j.gloplacha.2017.04.001
Mahowald, N. M., Muhs, D. R., Levis, S., Rasch, P. J., Masaru, Y., Zender, C. S., & Luo, C. (2006). Change in atmospheric mineral aerosols in response to climate: Last glacial period, preindustrial, modern, and doubled carbon dioxide climates. *Journal of Geophysical Research*, *111*(D10), D10202. https://doi.org/10.1029/2005JD006653
Matsumoto, K., & Gilchrist, M. D. (2022). MESMO global ocean model results for glacial and freshwater hosing simulations with calibrated, semilabile and refractory dissolved organic matter (Version 1) Version Date 2022-10-13 [Dataset]. Biological and Chemical Oceanography Data Management Office (BCO-DMO). https://doi.org/10.26008/1912/bco-dmo.882380.1
Matsumoto, K., Rickaby, R., & Tanioka, T. (2020). Carbon export buffering and CO_2 drawdown by flexible phytoplankton C:N:P under glacial conditions. *Paleoceanography and Paleoclimatology*, *35*(7), 1–22. https://doi.org/10.1029/2019PA003823
Matsumoto, K., Sarmiento, J. L., & Brzezinski, M. A. (2002). Silicic acid leakage from the Southern Ocean: A possible explanation for glacial atmospheric pCO_2. *Global Biogeochemical Cycles*, *16*(3), 5-1–5-23. https://doi.org/10.1029/2001GB001442
Matsumoto, K., Tanioka, T., & Zahn, J. (2021). MESMO 3: Flexible phytoplankton stoichiometry and refractory dissolved organic matter. *Geoscientific Model Development*, *14*(4), 2265–2288. https://doi.org/10.5194/gmd-14-2265-2021
Matsumoto, K., Tokos, K., Huston, A., & Joy-Warren, H. (2013). MESMO 2: A mechanistic marine silica cycle and coupling to a simple terrestrial scheme. *Geoscientific Model Development*, *6*(2), 477–494. https://doi.org/10.5194/gmd-6-477-2013
Matsumoto, K., Tokos, K., Price, A., & Cox, S. (2008). GENIE-M: A new and improved GENIE-developed in Minnesota. *Geoscientific Model Development Discussions*, *1*, 1–37. https://doi.org/10.5194/gmd-1-1-2008
Matsumoto, K., & Yokoyama, Y. (2013). Atmospheric $\Delta^{14}C$ reduction in simulations of Atlantic overturning circulation shutdown. *Global Biogeochemical Cycles*, *27*(2), 296–304. https://doi.org/10.1002/gbc.20035
McManus, J., Francois, R., Gherardi, J. M., Keigwin, L. D., & Brown-Leger, S. (2004). Collapse and rapid resumption of Atlantic meridional circulation linked to deglacial climate changes. *Nature*, *428*(6985), 834–837. https://doi.org/10.1038/nature02494
Molot, L. A., & Dillon, P. J. (1997). Photolytic regulation of dissolved organic carbon in northern lakes. *Global Biogeochemical Cycles*, *11*(3), 357–365. https://doi.org/10.1029/97GB01198
Mopper, K., Zhou, X., Kieber, R. J., Kieber, D. J., Sikorski, R. J., & Jones, R. D. (1991). Photochemical degradation of dissolved organic carbon and its impact on the oceanic carbon cycle. *Nature*, *353*(6339), 60–62. https://doi.org/10.1038/353060a0
Peltier, W. R., Liu, Y., & Crowley, J. W. (2007). Snowball Earth prevention by dissolved organic carbon remineralization. *Nature*, *450*(7171), 813–818. https://doi.org/10.1038/nature06354
Peltier, W. R. (1994). Ice age paleotopography. *Science*, *265*(80-), 195–201. https://doi.org/10.1126/science.265.5169.19
Porcal, P., Dillon, P. J., & Molot, L. A. (2015). Temperature dependence of photodegradation of dissolved organic matter to dissolved inorganic carbon and particulate organic carbon. *PLoS One*, *10*(6), 1–15. https://doi.org/10.1371/journal.pone.0128884
Redfield, A. C. (1934). *On the proportions of organic derivatives in sea water and their relation to the composition of plankton*. University Press of Liverpool. James Johnstone Memorial Volume. 11236440.

Roshan, S., & DeVries, T. (2017). Efficient dissolved organic carbon production and export in the oligotrophic ocean. *Nature Communications*, *8*(1), 2036. https://doi.org/10.1038/s41467-017-02227-3

Rothman, D. H., Hayes, J. M., & Summons, R. E. (2003). Dynamics of the Neoproterozoic carbon cycle. *Proceedings of the National Academy of Sciences of the United States of America*, *100*(14), 8124–8129. https://doi.org/10.1073/pnas.0832439100

Sexton, P. F., Norris, R. D., Wilson, P. A., Pälike, H., Westerhold, T., Röhl, U., et al. (2011). Eocene global warming events driven by ventilation of oceanic dissolved organic carbon. *Nature*, *471*(7338), 349–353. https://doi.org/10.1038/nature09826

Shen, Y., & Benner, R. (2018). Mixing it up in the ocean carbon cycle and the removal of refractory dissolved organic carbon. *Scientific Reports*, *8*, 1–9. https://doi.org/10.1038/s41598-018-20857-5

Smith, D. C., Simon, M., Alldredge, A. L., & Azam, F. (1992). Intense hydrolytic enzyme activity on marine aggregates and implications for rapid particle dissolution. *Nature*, *359*(6391), 139–142. https://doi.org/10.1038/359139a0

Swanson-Hysell, N. L., Rose, C. V., Calmet, C. C., Halverson, G. P., Hurtgen, M. T., & Maloof, A. C. (2010). Cryogenian glaciation and the onset of carbon-isotope decoupling. *Science*, *328*(5978), 608–611. https://doi.org/10.1126/science.1184508

Tanioka, T., & Matsumoto, K. (2017). Buffering of ocean export production by flexible elemental stoichiometry of particulate organic matter. *Global Biogeochemical Cycles*, *31*(10), 1528–1542. https://doi.org/10.1002/2017GB005670

Wagner, S., Schubotz, F., Kaiser, K., Hallmann, C., Waska, H., Rossel, P., et al. (2020). Soothsaying DOM: A current perspective on the future of oceanic dissolved organic carbon. *Frontiers in Marine Science*, *7*, 1–17. https://doi.org/10.3389/fmars.2020.00341

Walker, B. D., Primeau, F. W., Beaupre, S. R., Guilderson, T. P., Druffel, E. R. M., & McCarthy, M. D. (2016). Linked changes in marine dissolved organic carbon molecular size and radiocarbon age. *Geophysical Research Letters*, *43*(19), 10385–10393. https://doi.org/10.1002/2016GL070359

Wang, P., Li, Q., Tian, J., Jian, Z., Liu, C., Li, L., & Ma, W. (2014). Long-term cycles in the carbon reservoir of the quaternary ocean: A perspective from the South China sea. *National Science Review*, *1*, 119–143. https://doi.org/10.1093/nsr/nwt028

Weaver, A. J., Sedlá, J., Eby, M., Alexander, K., Crespin, E., Fichefet, T., et al. (2012). Stability of the Atlantic meridional overturning circulation: A model intercomparison. *Geophysical Research Letters*, *39*, 1–7. https://doi.org/10.1029/2012GL053763

Williams, P. M., & Druffel, E. R. M. (1987). Radiocarbon in dissolved organic matter in the central North Pacific Ocean. *Nature*, *330*(6145), 246–248. https://doi.org/10.1038/330246a0

Williams, R., & Follows, M. (2011). *Ocean dynamics and the carbon cycle: Principles and mechanisms*. Cambridge University Press. https://doi.org/10.1017/CBO9780511977817

Yamanaka, Y., & Tajika, E. (1997). Role of dissolved organic matter in the marine biogeochemical cycle: Studies using an ocean biogeochemical general circulation model. *Global Biogeochemical Cycles*, *11*(4), 599–612. https://doi.org/10.1029/97GB02301

Zakem, E. J., Cael, B. B., & Levine, N. M. (2021). A unified theory for organic matter accumulation. *Proceedings of the National Academy of Sciences of the United States of America*, *118*(6), e2016896118. https://doi.org/10.1073/pnas.2016896118

References From the Supporting Information

Anderson, L. A., & Sarmiento, J. L. (1994). Redfield ratios of remineralization determined by nutrient data analysis. *Global Biogeochemical Cycles*, *8*(1), 65–80. https://doi.org/10.1029/93GB03318

Berelson, W. M., Balch, W. M., Najjar, R., Feely, R. A., Sabine, C., & Lee, K. (2007). Relating estimates of $CaCO_3$ production, export, and dissolution in the water column to measurements of $CaCO_3$ rain into sediment traps and dissolution on the sea floor: A revised global carbonate budget. *Global Biogeochemical Cycles*, *201*, 1–15. https://doi.org/10.1029/2006GB002803

Carr, M. E., Friedrichs, M. A. M., Schmeltz, M., Noguchi Aita, M., Antoine, D., Arrigo, K. R., et al. (2006). A comparison of global estimates of marine primary production from ocean color. *Deep Sea Research Part II*, *53*(5–7), 741–770. https://doi.org/10.1016/j.dsr2.2006.01.028

DeVries, T., & Weber, T. (2017). The export and fate of organic matter in the ocean: New constraints from combining satellite and oceanographic tracer observations. *Global Biogeochemical Cycles*, *31*(3), 535–555. https://doi.org/10.1002/2016GB005551

Dunne, J. P., Sarmiento, J. L., & Gnanadesikan, A. (2007). A synthesis of global particle export from the surface ocean and cycling through the ocean interior and on the seafloor. *Global Biogeochemical Cycles*, *21*(4), 1–16. https://doi.org/10.1029/2006GB002907

Garcia, H. E., Weathers, K., Paver, C. R., Smolyar, I., Boyer, T. P., Locarnini, R. A., et al. (2019). World ocean atlas 2018, Volume 3: Dissolved oxygen, apparent oxygen utilization, and oxygen saturation. *NOAA Atlas NESDIS*, *3*, 38.

Landolfi, A., Kähler, P., Koeve, W., & Oschlies, A. (2018). Global marine N_2 fixation estimates: From observations to models. *Frontiers in Microbiology*, *9*, 1–8. https://doi.org/10.3389/fmicb.2018.02112

Martiny, A. C., Pham, C. T. A. A., Primeau, F. W., Vrugt, J. A., Moore, J. K., Levin, S. A., et al. (2013). Strong latitudinal patterns in the elemental ratios of marine plankton and organic matter. *Nature Geoscience*, *6*, 279–283. https://doi.org/10.1038/ngeo1757